FULL RESEARCH ARTICLE

Experimental and numerical investigations of the hot cracking susceptibility during the powder bed fusion of AA 7075 using a laser beam

Andreas Wimmer[1] · Hannes Panzer[1] · Christopher Zoeller[2] · Stefan Adami[3] · Nikolaus A. Adams[2,3] · Michael F. Zaeh[1]

Abstract

The variety of processable materials for the powder bed fusion of metals using a laser beam (PBF-LB/M) is still limited. In particular, high-strength aluminum alloys are difficult to process with PBF-LB/M without the occurrence of hot cracks. In situ alloying is a promising method to modify the physical properties of an alloy to reduce its hot cracking susceptibility. In this work, the aluminum alloy 7075 and blends with 2 wt.%, 4 wt.%, and 6 wt.% of Si were processed via PBF-LB/M. The Rappaz–Drezet–Gremaud (RDG) model and the Kou model were investigated regarding their capability of predicting the hot cracking behavior for the aluminum alloy 7075 and the three powder blends. The smoothed-particle hydrodynamics (SPH) method was used to gain the thermal input data for the RDG model. A clear tendency of a reduced hot cracking susceptibility with an increasing amount of Si was observed in the experiments and in the simulations. A detailed analysis of the type of the hot cracking mechanism in the aluminum alloy 7075 provided several indications of the presence of liquation cracking. The Kou model and the RDG model may be applicable for both solidification and liquation cracking. The presented methodology can be used to investigate any material combination and its susceptibility to hot cracking.

Keywords Additive manufacturing (AM) · Powder bed fusion · Smoothed-particle hydrodynamics (SPH) · In situ alloying · Simulation · Hot cracking

1 Introduction and state of the art

The powder bed fusion of metals using a laser beam (PBF-LB/M) has proven to be a suitable method for the manufacturing of structural parts with high geometric complexity [1]. Especially aluminum alloys (AA), with their key characteristics such as a low density in combination with a high strength [2], are promising materials for the automotive and aviation sectors [3].

The choice of AA that are processible by PBF-LB/M is still limited due to the formation of defects during the manufacturing process [4]. In particular, high-strength AA, such as the 7XXX series, which are of great industrial relevance, are difficult to process with PBF-LB/M without the occurrence of hot cracks [5]. A few alloys specifically designed for the PBF-LB/M process already exist, among them Scalmalloy or Addalloy, which are alternatives for high-strength 7XXX AA for specific applications. However, Rometsch et al. [6] discussed in their study that adding nanoparticles to a wrought 7XXX powder may achieve significantly higher yield strength values compared to the mentioned alternatives. The authors concluded that there is still a substantial need for printable high-strength AA.

A highly promising approach to influence the cracking susceptibility is to blend the powder with additives. Montero-Sistiaga et al. [7] increased the density of the AA 7075 alloy by adding Si, while Aversa et al. [8] showed

✉ Andreas Wimmer
  andreas.wimmer@iwb.tum.de

1 Institute for Machine Tools and Industrial Management, Technical University of Munich, Boltzmannstr. 15, Garching 85748, Germany

2 Chair of Aerodynamics and Fluid Mechanics, Technical University of Munich, Boltzmannstr. 15, Garching 85748, Germany

3 Munich Institute of Integrated Materials, Energy and Process Engineering, Technical University of Munich, Lichtenbergstr. 4a, Garching 85748, Germany

that introducing Ni strongly increases the hardness of an Al–Si–Ni alloy. Zhang et al. [9] demonstrated that the hot cracking susceptibility of an Al–Cu–Mg alloy can be significantly reduced by the addition of Zr. With this method, the thermo-physical properties and, thus, the cracking susceptibility of the solidifying melt pool can be modified by the addition of elements with different physical properties [10].

However, testing the effects of changes in the alloy composition on the hot cracking behavior consumes high amounts of powder and is associated with high experimental effort and costs. Using only experimental investigations, the transferability of the findings to other additives is difficult. To reduce the experimental effort and to achieve a physically based view of the hot crack formation process, a predictive simulation of the crack formation during the PBF-LB/M process is required.

In this work, the term *hot crack* is specified as a crack formed at temperatures near the completion of solidification [11]. In the following, hot cracking refers only to failures in the microdomain with liquid films present at the grain boundaries. Within this definition, the two relevant types of hot cracking are solidification cracking and liquation cracking.

Sun et al. [12] investigated the high-entropy alloy Co–Cr–Fe–Ni regarding its hot cracking susceptibility during PBF-LB/M via experimental and simulative approaches. Using atom probe tomography (APT), the authors revealed that no elemental segregation was present at intergranular cracks, which was reported by Chauvet et al. [13] as the cause of hot cracking. To quantify their observations, they used the Rappaz–Drezet–Gremaud (RDG) model. A new set of characteristic values for the depression pressure and the grain size were obtained, at which hot cracking is to be expected.

Dreano et al. [14] proposed a design procedure for a crack-free aluminum alloy for additive manufacturing relying on decreasing the brittle temperature range to mitigate the hot cracking. They added additional optimization criteria concerning the phase fractions and the solid solution strengthening to preserve the mechanical strength.

Sonawane et al. [15] set up a simulation model to predict the hot cracking susceptibility during PBF-LB/M for the AA6061. The hot cracks in the alloy were characterized via Scanning Electron Microscopy (SEM). A dendritic surface was detected, which was attributed to solidification cracking. Based on these findings, the RDG model was selected for the subsequent simulations. With this methodology, they determined a critical pressure drop, at which hot cracking is expected to occur.

Sonawane et al. [16] extended their approach by investigating the changes in the chemical composition of the AA6061. They varied the Si and Mg contents and studied the influence on the cracking behavior with their simulation approach. They showed that changing the Si content had no significant influence on solidification cracks. In contrast, the addition of Mg led to a reduced cracking susceptibility. The findings for the Si content, however, are not consistent with those from Montero-Sistiaga et al. [7] and Stopyra et al. [17] for AA 7075.

Regarding modeling of the melt pool during PBF-LB/M, several classical simulation approaches using Eulerian descriptions have been applied to PBF-LB/M in the past, e.g., by Sun et al. [18] and Koch et al. [19] using the volume-of-fluid method (VOF). However, considering the complex physics including multiple phase interfaces, phase change phenomena, variable surface tension, and violent interface deformation and fragmentation, these methods are strongly limited in their applicability by the nature of the schemes.

As a remedy, particle-based Lagrangian methods have gained strong interest as they are naturally suited for this application. Russell et al. [20] and Weirather et al. [21] demonstrated that the Smoothed-Particle Hydrodynamics (SPH) method is a viable and promising numerical tool for simulating the PBF-LB/M process. For a long time, one of the main obstacles to the breakthrough of the method was the high computational cost. Afrasiabi et al. [22] showed that an SPH implementation utilizing GPUs can significantly decrease the computational time of powder-scale SPH simulations. Another approach to perform multi-track simulations in a reasonable time was presented by Fürstenau et al. [23] and Lüthi et al. [24]. In their work, a full spatial adaptivity was enabled by a splitting and merging of particles, while a simultaneous refining and coarsening of the spatial resolution was possible for multiple times.

1.1 Research questions

In conclusion with regard to the state of the art, only limited knowledge exists about the hot crack formation in general, and in particular for the AA 7075, during the PBF-LB/M process. This raises the following research questions:

- What are appropriate hot cracking models for predicting the failure behavior during PBF-LB/M, and when should they be applied?
- How precise is the prediction of the hot cracking susceptibility with thermal calibration data originating from physically based process models?
- What type of hot crack is present in the AA 7075 when manufactured by PBF-LB/M?
- What is the effect of Si addition on the hot cracking susceptibility of AA 7075?

1.2 Approach

In this work, the hot cracking susceptibility of the research-relevant AA 7075 was studied for the PBF-LB/M process. Two appropriate hot cracking models were selected and implemented in the authors' existing SPH framework [21, 25]. To ensure a realistic mapping of the process, single-track simulations were performed to obtain thermal data from the PBF-LB/M process to serve as input for the hot cracking models. The single-track simulations of the AA 7075 were compared to experimental data for three different parameter settings. The validated simulation model was then further used to investigate its capability of simulating the in situ alloying and its application to reduce the hot cracking susceptibility. The additive Si was selected, and three blends of the modified AA 7075 were then processed using PBF-LB/M. The prediction of the hot cracking susceptibility of the two models was then compared with the experimental data. Subsequently, the type of the crack was analyzed, and the applicability of the two hot cracking models was discussed.

2 Materials and experimental methods

This section gives a detailed description of the powder blending and the experimental setup used in this work.

2.1 Powder

According to the presented state of the art, the addition of Si to aluminum alloys is highly attractive for reducing hot cracking. The experiments in this work were conducted with a AA 7075 powder (Poudres Hermillon, France) and with blends containing the AA 7075 as the base powder and 2 wt.%, 4 wt.%, and 6 wt.% of Si (US Research Nanomaterials, USA) as additive. The chemical composition of the AA 7075 is given in Table 1.

The Si powder had a purity of 99.995 %. Particle-size distribution (PSD) measurements were performed using a particle analyzer (Camsizer X2, Retsch, Germany), which is based on a dynamic image analysis, and yielded $D_{10} = 29.3$ μm, $D_{50} = 48.7$ μm, and $D_{90} = 97.6$ μm for the base powder, and $D_{10} = 3.3$ μm, $D_{50} = 6.1$ μm, and $D_{90} = 9.0$ μm for the Si additive. The mixing was performed with a roller mixer (RM 2, Edmund Buehler, Germany). The blends with 2 wt.% and 4 wt.% Si were mixed for 1 h, while the blend with 6 wt.% Si was mixed for two hours to avoid agglomerations of the Si particles.

When blending a base powder with additive particles, an even distribution of the additives must be ensured. For this work, this is particularly important in order not to over- or underestimate the hot cracking behavior of the modified alloy due to an accumulation of the Si additive. Figure 1 shows an exemplary SEM image of the powder blend with AA 7075 and 2 wt.% of Si. The figure shows that the smaller Si particles were adsorbed homogeneously to the bigger AA 7075 particles, which indicates an overall homogeneous distribution.

2.2 PBF-LB/M setup

When using various process parameters, several powder mixtures, and different types of scanning strategies, the experimental setup must have a high degree of flexibility. Therefore, a novel PBF-LB/M test bench [26, 27] was utilized (see Fig. 2).

The test bench consisted of a 1000 W fiber laser (YLR-1000-WC-Y14, IPG Laser, Germany), a chiller (P300, Termotek, Germany), a self-built PBF-LB/M chamber, and an optical setup. The optical setup included a breadboard (Thorlabs, USA), on which several optical instruments were mounted and aligned for an open beam path. The beam was expanded by a collimator (D50-F200, IPG Laser, Germany) and then guided through the scanning systems for area irradiation (intelliSCAN III30, Scanlab, Germany) and beam
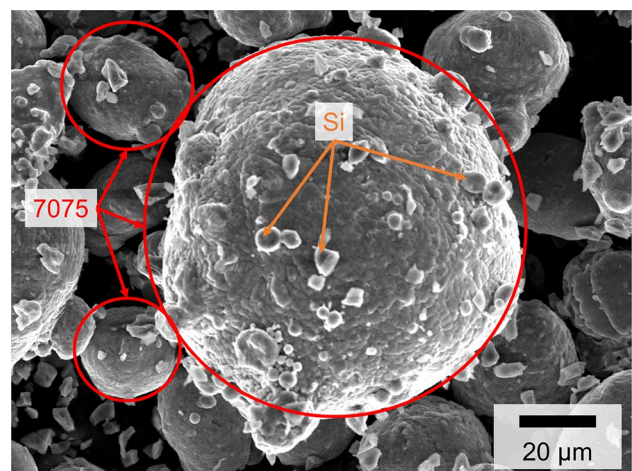

Fig. 1 SEM image of the powder blend consisting of AA 7075 as the base powder (big grey particles) and 2 wt.% Si as the additive (small white particles)

Table 1 Chemical composition of the AA 7075 used in this work

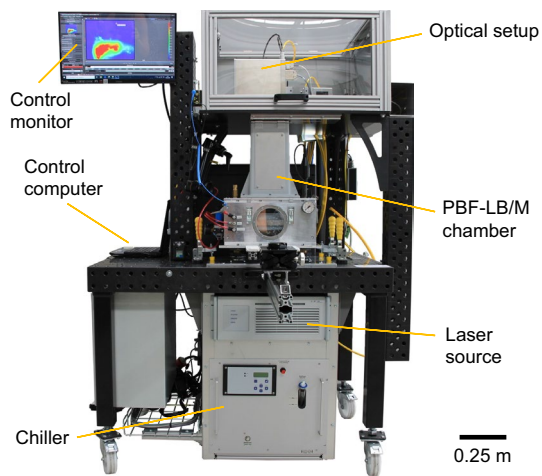| Element	Al	Fe	Si	Mn	Zn	Mg	Cu	Cr	Ti	Ni	Ga	V
Amount in wt.%	89.60	0.10	0.39	<0.01	5.90	2.30	1.50	0.22	<0.01	<0.01	0.01	<0.01

Fig. 2 Experimental setup for the PBF-LB/M process

waist variation (varioSCAN de40i, Scanlab, Germany). The test bench enabled the fabrication of single as well as multiple powder layers over an area of 32×70 mm^2. Therefore, the amount of powder needed for the experiments was comparatively small, which made the setup well-suited for investigating different powder mixtures.

In this work, single-track as well as multi-layer experiments were conducted. Preliminary studies were performed using the parameter set of [17] as a starting basis to find an appropriate process parameter set for the AA 7075. Single weld lines were analyzed via optical microscopy to identify the set with the most consistent and reproducible solidified tracks. The process parameters utilized for both the experiments and the simulations are listed in Table 2.

2.3 Characterization of the samples

The equipment used for the characterization of the single tracks and the cubes is specified in the appendix (Table 6). For the micrographs, the specimens were cut perpendicular to the scanning direction of the laser beam, ground, and polished with a 1 μm diamond paste. The samples were etched with an etching agent based on Kroll.

Regarding the SEM and the scanning transmission electron microscopy (STEM), the following parameters were applied: The acceleration voltage of the SEM was set to 15 kV. A probe current of 60 nA was chosen for the powder investigations and 68 nA for the metallographic preparations. For the STEM, an acceleration voltage of 30 kV was used.

3 Numerical modeling

This section presents two suitable hot cracking models and details of the numerical setup used in this work.

3.1 Hot cracking models

The main requirements for an appropriate model that is capable of characterizing both hot cracking and in situ alloying, allowing a transferability of the results, can be stated as

- Accounting for a change in the hot cracking behavior due to changes in the chemical composition and
- To be physics based.

After evaluating various hot cracking models from the literature, the following two models were chosen for a further evaluation as they fulfill the stated requirements.

RDG model. Rappaz et al. [28] proposed that hot cracking is preceded by microvoid formation. The void is assumed to be formed due to a high strain rate generated by a thermal expansion perpendicular to the dendrite axes. A pressure drop close to the root of the dendrites is generated due to the resulting deformation. The molten phase then fills the created spaces. Because of premature solidification, a complete compensation might not be ensured, leading to micropores and, therefore, to hot cracking.

The RDG model reads [29]

$$\dot{\varepsilon}_{\text{d, max}} = \frac{|\nabla T|}{B(T)} \left(\frac{\lambda^2 |\nabla T| \Delta p_{\text{c}}}{180(1+\beta)\eta} - \frac{v_{\text{iso}}\beta H(T)}{1+\beta} \right), \quad (1)$$

where $\dot{\varepsilon}_{\text{d, max}}$ describes the maximum strain rate of the dendrites, T the temperature with $|\nabla T|$ the absolute value of the

Table 2 PBF-LB/M parameters for the conducted single-track experiments and single-track simulations, as well as for the cubic samples in the experiment

Property	Experiment	Simulation	Unit
Laser power	300	300	W
Scanning velocities (single tracks)	225, 500, and 800	225, 500, and 800	mm/s
Scanning velocity (cuboids)	225	–	mm/s
Laser spot radius	40	40	μm
Layer height	30	30	μm
Hatch spacing (cuboids)	140	–	μm
Volume (cuboids)	$5 \times 5 \times 0.5$	–	mm^3
Exposure patterns (cuboids)	meander	–	–

thermal gradient, λ represents the secondary dendrite spacing, and β the shrinkage factor, defined as $\beta = \rho_S / \rho_L - 1$ with ρ_S and ρ_L as the density of the solid and the liquid, respectively. η describes the dynamic viscosity and Δp_c the critical pressure drop, at which the microvoid formation is to be expected. v_{iso} is the velocity of the isotherms, and T_S and T_L are the temperature at the end of the solidification and the liquidus temperature, respectively.

The temperature-dependent functions $B(T)$ and $H(T)$ are defined as

$$B(T) = \int_{T_S}^{T_L} \frac{\int_{T_S}^{T_L} f_S(T)\mathrm{d}T f_S(T)^2}{(1 - f_S(T))^3} \mathrm{d}T \text{ and,} \tag{2}$$

$$H(T) = \int_{T_S}^{T_L} \frac{f_S(T)^2}{(1 - f_S(T))^2} \mathrm{d}T , \tag{3}$$

where $f_S(T)$ is the solid fraction. Assuming that the strain rate is independent of the temperature in the given temperature interval [29–31], a closed-form solution for the critical strain rate $\dot{\varepsilon}_{d,max}$ can be obtained. The main outcome of the RDG model is the hot cracking susceptibility HCS_{RDG}, which Rappaz et al. [28] defined as

$$HCS_{RDG} \sim \frac{1}{\dot{\varepsilon}_{d,\ max}} . \tag{4}$$

Kou model. Kou [32] developed a criterion for the hot crack formation, which was concretized and applied to various materials [33]. Within this cracking model, the separation of grains from each other is caused by tensile deformation, the growth in the lateral direction towards each other is caused by solidification processes, and the feeding between the grains by liquid is caused by shrinkage.

The criterion characterizing the susceptibility to the crack formation was introduced as the maximum steepness of the curve in a T-$f_S^{1/2}$-diagram up to a certain threshold. The Kou criterion for the hot cracking susceptibility HCS_{Kou} reads

$$HCS_{Kou} \sim \max\left(\left|\frac{\mathrm{d}T}{\mathrm{d}f_s^{1/2}}\right|\right) . \tag{5}$$

Blending the powder with additives alters the solidification path and, therefore, leads to a variation in the hot cracking susceptibility. In this work, this correlation was used for a relative comparison of the hot cracking susceptibility between the different powder blends.

Considering the equations and statements above, the main input parameter for both models (RDG and Kou) is the solid fraction in the mushy zone as a function of the temperature. The solidification paths of the AA 7075 and the powder blends containing different amounts of Si were determined

by the software Thermo-Calc (Thermo-Calc Software, Sweden). To determine the necessary values for the temperature gradients, the SPH method was applied. In contrast to analytical modeling of the process zone, the SPH method includes various physical phenomena of the melting process that took place prior to the solidification, which significantly impacts the temperature gradient.

3.2 Numerical setup

In this work, the Lagrangian advanced manufacturing simulator (LAMAS) of the Chair of Aerodynamics and Fluid Mechanics was used to perform single-track simulations of the PBF-LB/M process to generate single track temperature data to serve as an input for the RDG model. The numerical model was based on the weakly compressible multi-phase formulation from Hu and Adams [34], enhanced by the transport-velocity formulation of Adami et al. [35]. Evaporation effects on the melt dynamics were incorporated by the recoil pressure model [21]. In the energy balance, the conduction, the convective cooling, the evaporative cooling, and the phase change including latent heat were considered [21, 36, 37]. The laser model of Weirather et al. [21] was used, where energy deposition is applied at the material surface only. Boundary conditions were set via dummy particles following Adami et al. [38]. The powder particle distribution was generated by the drop-and-roll algorithm from Zhou et al. [39]. With regard to the experimental validation, a similar PSD with powder particle sizes between 10 μm and 30 μm was used. This powder layer was applied atop an AA 7075 base plate both in the experiment and in the simulation. The code built on OpenFPM, a scalable and open C++ framework for parallel particles and mesh simulations on both CPU and GPU architectures [40]. The parameters of the SPH simulations are listed in Table 3. The given set of equations are advanced in time using an explicit velocity Verlet time integration scheme [41]. The maximum time step size of 12.05 ns was determined by the most restrictive stability condition among viscosity, surface tension, recoil pressure, thermal conduction, and CFL number (Courant–Friedrichs–Lewy number) [42–45]. Each simulation

Table 3 Parameters of the SPH simulations

Property	Value	Unit
Domain size	$860 \times 600 \times 260$	μm^3
Particle spacing	4	μm
Number of particles	2,096,250	–
Kernel type	Quintic spline	–
Reference length	24	μm
Reference velocity	5	m/s
Time step	12.05	ns

was conducted on 112 CPU cores with nominal frequencies of 2.6 GHz. The computational time for simulating a physical time of 625 µs was 4,144 CPU hours.

3.3 Material parameters

To predict the cracking susceptibility of the AA 7075 by means of the two hot cracking models, the corresponding material parameters were taken from the literature and are listed in the appendix (Tables 5, 8). Parameters that could not be extracted directly from literature were approximated with weighted values according to the percentage of the chemical elements in the AA 7075 [21]. This procedure was used for the boiling temperature, the molar heat of evaporation, the specific heat of evaporation, and the molar mass. For the powder blends, the parameters were weighted according to the amount of the Si additive.

The absorptivity a was calculated using the equation from Bramson [46] as a function of the electrical resistivity ρ_{el} of the material and the wavelength λ of the laser:

$$a \approx 0.365 \cdot \left(\frac{\rho_{el}}{\lambda}\right)^{\frac{1}{2}} - 0.0667 \cdot \left(\frac{\rho_{el}}{\lambda}\right) + 0.006 \cdot \left(\frac{\rho_{el}}{\lambda}\right)^{\frac{3}{2}}. \tag{6}$$

The electrical resistivity of the AA 7075 was determined by weighting, using its elemental values from Valencia and Quested [47]:

$$\rho_{el,S} = 11.38 \ \mu\Omega \cdot cm \quad \text{for the solid and} \tag{7}$$

$$\rho_{el,L} = 25.33 \ \mu\Omega \cdot cm \quad \text{for the liquid.} \tag{8}$$

The absorptivities for the solid and liquid phases a_S and a_L, respectively, with a laser wavelength of 1064 nm, can then be determined as

$$a_S \approx 0.11 \quad \text{and} \tag{9}$$

$$a_L \approx 0.16. \tag{10}$$

As the applied laser model disregards multi-reflections in the melt pool vapor capillary, an effective absorptivity was used in the simulations. A calibration with the experimental melt pool dimensions yielded a scaling coefficient of 1.56, which was applied to the physical absorptivity values (see Tables 5, 8 in the appendix). The value for the boiling enthalpy was determined through linear extrapolation of the enthalpy values from Mills [48]. The experiments were conducted using Argon as process gas. The parameters used for Argon are listed in Table 7 in the Appendix.

The solid fraction as a function of the temperature for the AA 7075 was determined by the software Thermo-Calc (version 2022a, TCAL2 database), which utilizes the CALPHAD method [49]. The conditions of Scheil [50] and

Gulliver [51] were applied, which assume an infinitely fast diffusion in the liquid, negligible diffusion in the solid, and an equilibrium at the solid–liquid interface.

The selection of the solid fraction at which solidification cracking occurs is controversially discussed in the literature. Some researchers showed that during cracking, the solid fraction is in the late stages of the solidification, i.e., between 0.85 and 0.95 [52, 53]. However, other works reported that solidification cracking occurred shortly before the end of the solidification, i.e., for solid fractions higher than 0.95 [54, 55]. As proposed by several researchers, the range where cracking is to be expected is the brittle temperature range (BTR) [32, 56, 57]. In this work, the two solid fraction values of $f_S = 0.87$ and $f_S = 0.94$ were used for the BTR, similar to Bodaghi et al. [58]. By means of the solidification path, these values can be directly correlated to the coalescence temperature and coherence temperature [59]. The remaining parameters for the cracking model are provided in Table 4.

3.4 Verification

The simulation was verified for both the discretization with SPH particles and the implementation of the RDG model. Due to its analytical nature, the Kou model was not verified. A convergence study of the SPH particle spacing yielded a sufficiently small variation in the melt pool geometry for a particle spacing from 4 µm to 3 µm. Therefore, an SPH particle spacing of 4 µm was applied in all simulations. The implementation of the RDG model was verified by the simplified assumption of an analytical function for $f_S(T)$. To consider the errors in the numerical integration, the nonlinear function $f_S(T) = 1 - T^2$ was chosen. Figure 3 depicts the hot cracking susceptibility of the dendrites over the norm of the temperature gradient. The numerical implementation of the RDG model and the analytical RDG model agree very well, indicating a correct model implementation.

4 Results

This section is divided into three parts: first, the results of single-track simulations and experiments of the AA 7075 are compared regarding the melt pool dimensions; second, the hot cracking susceptibility of the powder blends,

Table 4 List of model parameters [28]

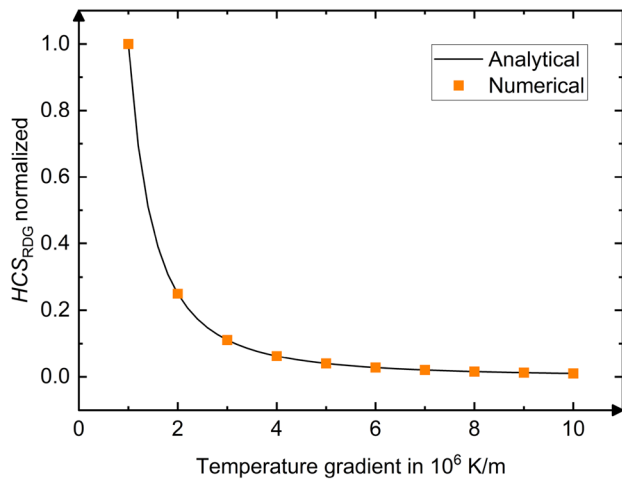| Parameter	Symbol	Value	Unit
Cavitation depression	Δp_c	$2 \cdot 10^3$	Pa
Velocity of isotherms	v_{iso}	$1 \cdot 10^{-4}$	m/s
Secondary arm spacing	λ_2	$100 \cdot 10^{-6}$	m

Fig. 3 Verification of the RDG model; the non-linear analytical function $f_S(T) = 1 - T^2$ was chosen for the verification of the RDG model

Fig. 4 Exemplary single-track PBF-LB/M simulation of the AA 7075 by means of SPH; the postprocessing was performed with Paraview (Version 5.11, Sandia National Laboratories, USA)

consisting of the AA 7075 and the Si additive, are compared between the simulation and the experiment; third, the hot cracks are characterized experimentally to identify the crack formation process.

4.1 Comparison of the melt pool dimensions

To demonstrate that the SPH simulation achieves reliable results when simulating the AA 7075, single-track simulations were performed with three different parameter settings (see Table 2). An exemplary image of a single-track PBF-LB/M simulation with LAMAS is depicted in Fig. 4.

A total of six single tracks were performed in the experiment, whereby eight micrographs were performed for each single track. The quantitative comparison between the experiment and the simulation is depicted in Fig. 5. The tendency of decreasing widths and depths of the melt pool with increasing scanning velocities is consistent with observations for other materials, i.e., for the Ti–6Al–4V alloy [60] and for the stainless steel 316 L [61]. The simulation results agree well with the experimental observations, both, qualitatively and quantitatively. The standard deviations of the melt pool width and depth overlap with all simulation results. However, at the low scanning velocity of 225 mm/s, a slight underestimation of the SPH simulation is observed. Since the scanning velocity of 225 mm/s is close or even within the transition region, a more pronounced vapor cavity and, in turn, multi-reflections occur, which are neglected by the current model. With increasing scanning velocities, this effect becomes negligible, since less energy is introduced per surface area. The better matching of the data points for increasing
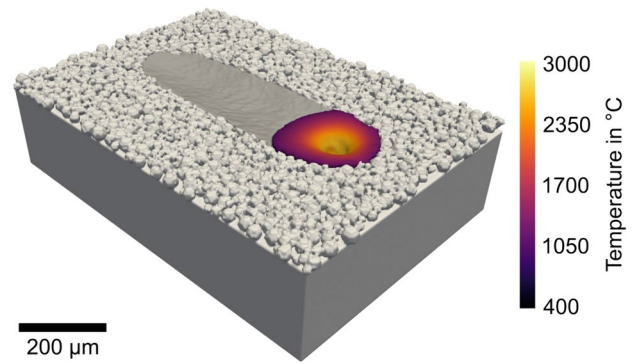
scanning velocities between simulation and experiment in Figure 5 supports this assumption.

4.2 Comparison of the hot cracking susceptibility

To alter the hot cracking susceptibility, the AA 7075 powder was blended with 2 wt.%, 4 wt.%, and 6 wt.% Si. In this subsection, the experimental and the numerical results for the hot cracking susceptibilities of these blends are presented and discussed.

Experimental results. Cuboids of $5 \times 5 \times 0.5 \text{ mm}^3$ were manufactured for each powder blend (the detailed parameters are listed in Table 2). Figure 6 shows micrographs of the pure AA 7075 and Si-containing samples. A qualitative examination of the results shows that the sample with the
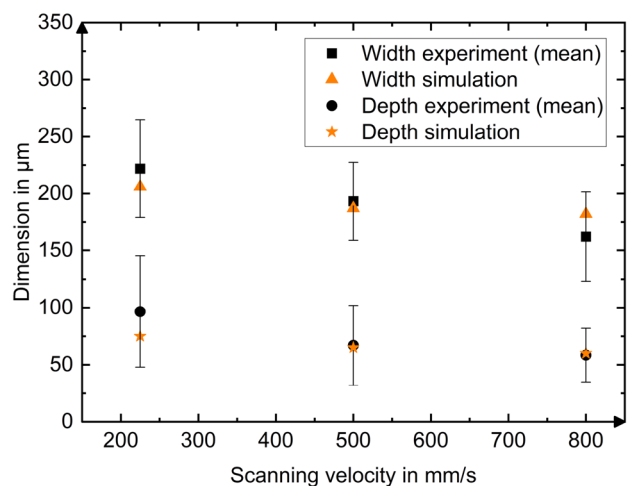

Fig. 5 Comparison of the melt pool width and depth between the simulation and the experiment for the AA 7075 with a constant laser power of 300 W and a scanning velocity of 225 mm/s; the error bars indicate the standard deviations

pure AA 7075 exhibits a high quantity of hot cracks, while the samples with increasing Si content show a decreasing number of this type of defect. This observation is consistent with Otani and Sasaki [62]; however, the authors observed crack-free samples only at 5 wt.% Si and above. In addition to the cubic samples, single tracks of the AA 7075 were examined regarding the location of the hot cracks. It was observed that hot cracks tend to form in the center of a single track. Figure 7 shows an exemplary cross-sectional micrograph of a single track with a hot crack in the center.

Numerical results. The determination of the hot cracking susceptibility via the RDG model consisted of three steps: first, the SPH simulation was used to simulate the melt pool during a single track for the different powder blends; second, the temperature gradients occurring in the mushy zone were determined; third, the temperature gradients were used as input for the RDG model to determine the local hot cracking susceptibility for every SPH discretization particle.

Figure 8 shows the results for the pure AA 7075 and the different powder blends. Here, all SPH particles with a hot cracking susceptibility greater than zero are taken into account at the time $t = 2.2$ ms with a melt pool being in a
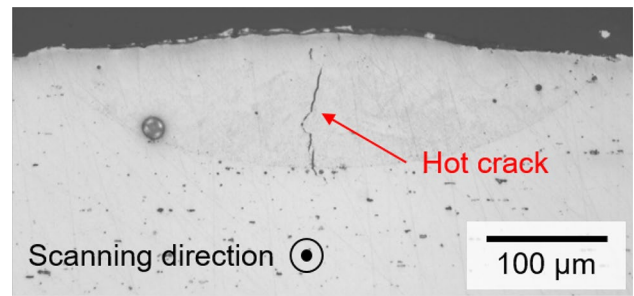

Fig. 7 Exemplary cross section of a single track; the borders of the solidified melt pool as well as a hot crack in the center of the track are clearly visible

steady state. The mean hot cracking susceptibility decreases for increasing amounts of Si.

In addition to determine the hot cracking susceptibility of the entire melt pool, the locality of a possible hot cracking occurrence was also identified. Figure 9 depicts a snapshot from the SPH simulation at $t = 2.2$ ms. The snapshot shows high hot cracking susceptibilities in the center of the tail and decreasing values towards the outside. The high hot

Fig. 6 Cross sections showing the cracking susceptibility with increasing Si contents; while the AA 7075 sample in (**a**) with 0 wt.% Si exhibits a high number of hot cracks, the samples depicted in (**b–d**) show a decreasing trend of cracks

a) 7075 with 0 wt.% Si

b) 7075 with 2 wt.% Si
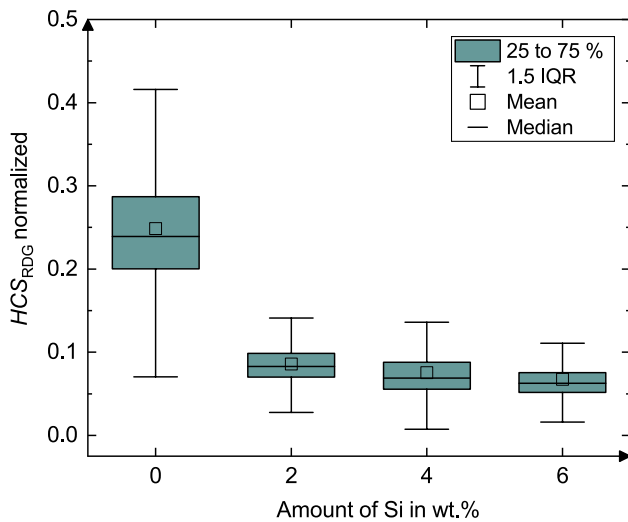
c) 7075 with 4 wt.% Si

d) 7075 with 6 wt.% Si
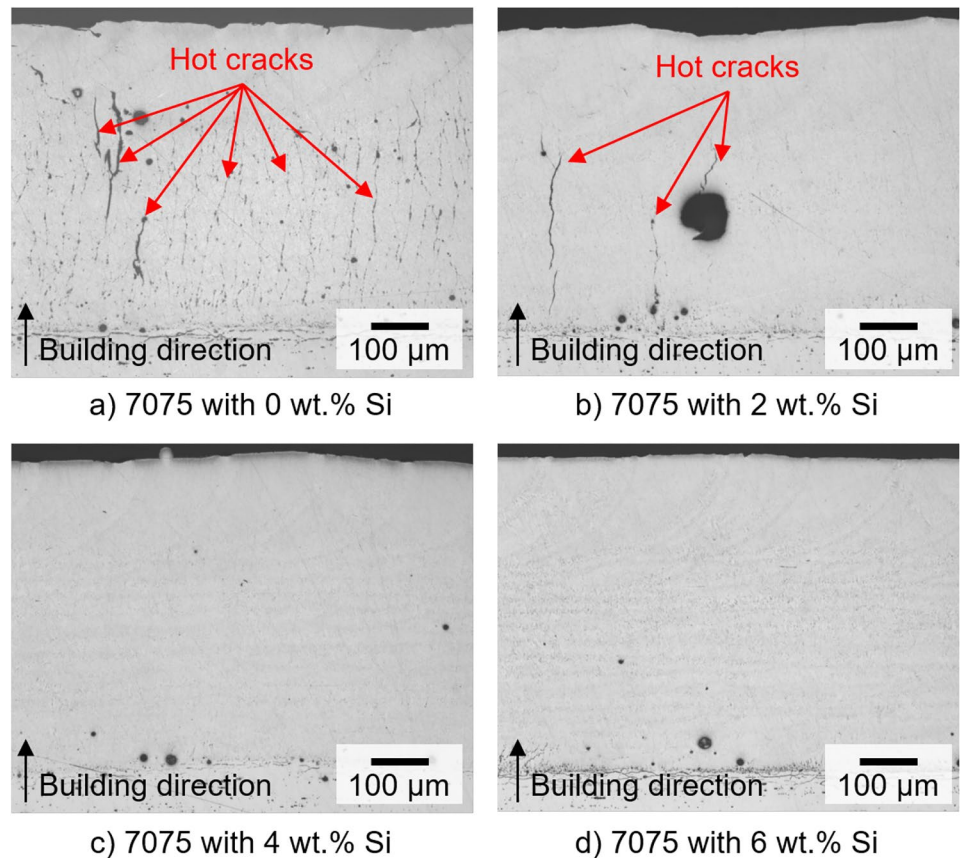
Fig. 8 Box plot of the hot cracking susceptibility predicted by the RDG model at $t = 2.2$ ms; the error bars indicate the interquartile range (IQR)
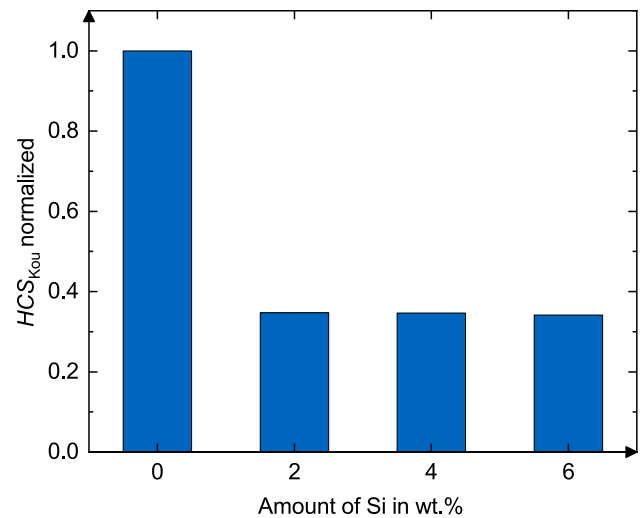

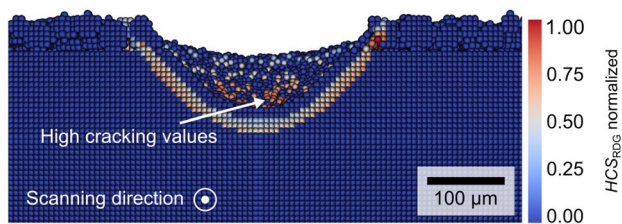Fig. 10 Hot cracking susceptibility predicted by the Kou model until $f_s^{1/2} = 0.97$

Fig. 9 Exemplary cross section of a single-track SPH simulation of the AA 7075 during the PBF-LB/M process; high cracking values are visible in the middle of the melt pool tail; the postprocessing was performed with Paraview (Version 5.11, Sandia National Laboratories, USA)

cracking susceptibilities in the top right (partially melted powder particle) are attributed to SPH particles that are in the heating phase; however, the RDG model is only valid in the cooling phase.

For the Kou model, the hot cracking susceptibilities were calculated according to Eq. 5 for the pure AA 7075 and for the powder blends. Similar to Kou [33], the maximum steepness of the curve in the T-$f_S^{1/2}$-diagram was evaluated until $f_S^{1/2} = 0.97$. Figure 10 shows a decrease in the hot cracking susceptibility of ≈ 65 % when adding 2 wt.% Si. The addition of 4 wt.% and 6 wt.% Si changes the HCS only slightly compared to the 2 wt.% Si.

Discussion. Due to the good agreement with the experimental observations, it can be stated that both models

are capable of predicting the decrease in the hot cracking susceptibility with increasing amounts of Si. As opposed to the simple hot cracking index from Kou [32], the hot cracking index proposed by Rappaz et al. [28] additionally provides information about the location of the hot crack. The comparison with the experimental results shows good agreement for the cracking localization. The significantly increased implementation and computation effort of the RDG model compared to the simple Kou model can be justified if detailed information about the crack initiation process within the weld bead is of interest. The RDG model may also be utilized to increase the process understanding of the intrinsic cracking phenomena. If only the processability of an alloy with a changing chemical composition needs to be investigated, the Kou model provides satisfactory results.

The observation of the decrease in the HCS for increasing Si contents can be explained by a binary Al–Si phase diagram, shown in Fig. 11. There, a tie line is drawn horizontally from liquid to solid at a specific temperature for an exemplary composition. The mass fraction of point B at the solidus is given by wt.$_S$ and at the liquidus by wt.$_L$. According to the lever rule [63], the amount of liquid increases with increasing Si content at a given temperature, which favors inter-dendritic feeding resulting in a reduced HCS.

To determine if parts have or do not have hot cracks for a specific amount of additive, the hot cracking
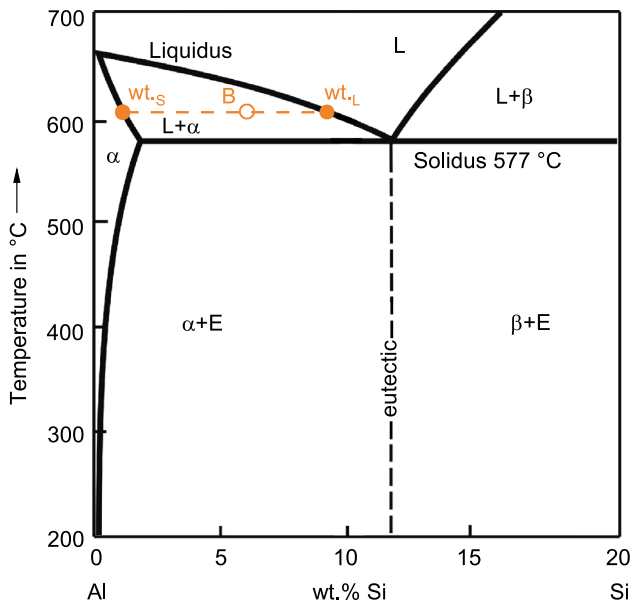
Fig. 11 Binary Al–Si phase diagram adapted from Massalski and Okamoto [64]; the dashed orange line represents the tie line for the lever rule; at a given point B, the mass fraction of the liquid is given by $wt._L$ and the of the solid by $wt._S$

susceptibilities of both models need to be calibrated to obtain absolute values. One way would be to quantify the number of hot cracks in micrographs for several powder blends. In the case of this work, from 4 wt.% Si upwards the samples can be considered as free of hot cracks. The corresponding hot cracking susceptibility could then be calibrated for this amount of Si. However, the amount of added Si may differ for a crack-free sample [62] and should therefore be determined specifically for each powder blend and experimental setup. Moreover, the size and the geometry of the printed part may influence the amount of additives since both variables affect the temperature gradient, the melt pool dimensions, and the mushy zone. If, for example, the geometry of a part leads to a heat accumulation below the melt pool, the liquid in the melt pool may persist for a longer period of time and thus favors inter-dendritic feeding.

4.3 Experimental characterization of the hot cracks

To study the type of the cracking mechanism in the AA 7075, detailed investigations of the cracks by various microscopic approaches were conducted and their results are presented in the following.

A significantly reduced number of cracks were detected on the upper part of the additively manufactured samples,
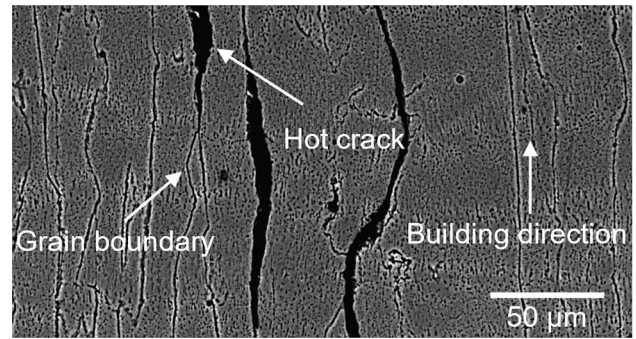

Fig. 12 SEM picture of the AA 7075 sample; the hot cracks (black elongated areas) tend to form along the grain boundaries (thin grey lines)

corresponding to the area penetrated by the last laser hatching (see Fig. 6 a)). This is an indicator that the type of crack present is liquation cracking, as it is known to form in the partially melted zone and the heat-affected zone [11].

Further investigations of the hot cracks by SEM revealed that the cracks formed along the grain boundaries (see Fig. 12). While this is a characteristic of both solidification and liquation cracking, no liquid back-filling effects at the crack tips were detected. This observation supports the previous statement about the presence of liquation cracking.

The hot cracks were also examined by STEM (see Fig. 13). The image shows another indication that liquid had
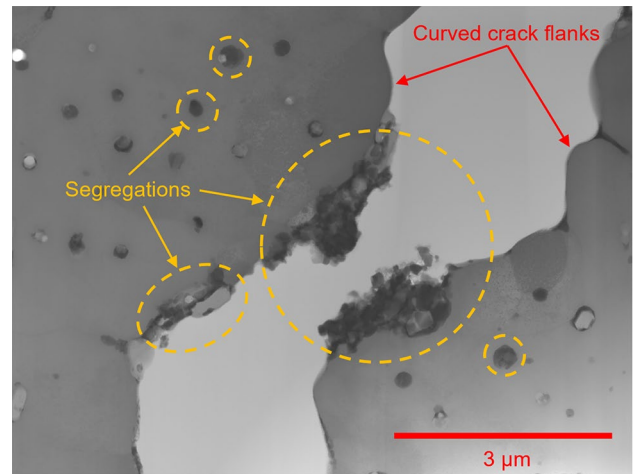

Fig. 13 STEM image of a crack of the AA 7075 sample; in close proximity to the curved crack flanks, segregations can be identified (highlighted with dashed orange lines); EDX analysis showed an increased amount of Cu, Mg, Zn, and Si within these segregations

to be present immediately before the crack formed, as the contour of the crack flanks is curved. In the center of Fig. 13 and in close proximity to the crack flanks, segregations could be identified. Energy-dispersive X-ray (EDX) analysis showed that these spots exhibited an increased amount of Cu, Mg, Zn, and Si, which are the main alloying elements of the AA 7075. Considering the fact that Mg and Zn have a lower melting point than Al [47], the hot crack formation may be attributable to the penetration or segregation mechanism. According to Lippold [11], the penetration mechanism is characterized by three events. First, a local liquation in the microstructure occurs. Outside the grain boundaries, a particle undergoes constitutional liquation due to a reduced melting temperature compared to the surrounding matrix. Second, a thermally driven grain growth and, therefore, a grain boundary movement takes place. Third, the liquid must be able to wet the boundaries surrounding the grains. Considering the segregation mechanism, the grain boundaries are enriched with elements reducing the melting temperature. An increase in the concentration of these elements is realized due to diffusion or segregation at the boundaries at elevated temperatures. Both mechanisms seem to be appropriate means to describe the crack formation due to an agglomeration of Mg and Zn within the AA 7075 during the PBF-LB/M process. Especially the latter element, which is one of the key components of the aluminum alloy to increase the strength of the material, seems to be the main source of the liquation crack formation due to its significantly lower melting point compared to the surrounding aluminum.

As a conclusion regarding the type of hot crack in the AA 7075, it can be stated that the various microscopic observations described above indicate the presence of liquation cracking. To the best of the authors' knowledge, the type of crack in the AA 7075 has been attributed to hot cracking in general without further differentiation [5, 7] or to solidification cracking [17].

Despite the presence of liquation cracks within the PBF-LB/M processed AA 7075, both models, Kou and RDG, predict the correct material behavior. This might be an indication that the models are capable of predicting both solidification and liquation cracking.

5 Conclusions and outlook

In this work, the hot cracking of the research-relevant AA 7075 was studied for the PBF-LB/M process. The additive Si was selected, and three blends of the modified

AA 7075 were processed using PBF-LB/M. Two models, namely RDG and Kou, were tested for their prediction capabilities of the hot cracking susceptibility of the AA 7075. An SPH simulation model was used to predict the temperature gradients in the mushy zone of the melt pool, which served as an input to the RDG model. The melt pool dimensions of the AA 7075 and the prediction of the hot cracking susceptibility were compared with experimental data. Subsequently, the type of crack was analyzed, and the applicability of the hot cracking models was discussed. The main findings are:

- When adding ≥ 4 wt.% of Si to the AA 7075, crack-free samples could be produced.
- The approach of combining the SPH simulation with the RDG model was successful, as the prediction of the hot cracking susceptibility and the location of high cracking values agreed very well with the experimental results.
- If only the processability of an alloy with a changing chemical composition needs to be investigated, the Kou model provides satisfactory results with less computational effort.
- A detailed analysis of the type of hot cracking mechanism provided several indications of the presence of liquation cracking.
- The Kou model and the RDG model may be applicable for both solidification and liquation cracking.

The presented methodology can be used to investigate any material combination and its susceptibility to hot cracking. Note that the RDG model is only capable of predicting the onset of a crack. The model does not consider the inherent heat treatment due to a repetitive melting of powder layers during the PBF-LB/M process. This characteristic has an influence on the crack length and, therefore, on the crack propagation mechanism, but also on potential crack healing effects. By using a multi-scale approach to simulate several layers, the effects of emerging hot cracks could be analyzed at the part scale.

Appendix A

See Tables 5, 6, 7 and 8.

Table 5 Material properties of the AA 7075

Symbol	Property	Value	Unit	References
ρ_S	Density (solid)	2800	kg/m^3	[47, 65, 66]
ρ_L	Density (liquid)	2500	kg/m^3	[47]
T_S	Solidus temperature	753.15	K	[65]
T_L	Liquidus temperature	901.0	K	[47]
T_B	Boiling temperature	2626.82	K	[67]
k_S	Thermal conductivity (solid)	160	W/(m·K)	[65, 66]
k_L	Thermal conductivity (liquid)	85	W/(m·K)	[47]
H_L	Enthalpy of fusion	$358 \cdot 10^3$	J/kg	[47]
H_B	Boiling enthalpy	$2946.39 \cdot 10^3$	J/kg	[48]
$c_{p,S}$	Specific heat capacity (solid)	860	J/(kg·K)	[47, 65, 66]
$c_{p,L}$	Specific heat capacity (liquid)	1130	J/(kg·K)	[47]
η	Dynamic viscosity	$1.2 \cdot 10^{-3}$	Pa·s	[47]
α	Surface tension coefficient	0.914	N/m	[47]
H_{spec}	Specific heat of evaporation	$9808.12 \cdot 10^3$	J/kg	[67]
H_{molar}	Molar heat of evaporation	$271.644 \cdot 10^3$	J/mol	[67]
M	Molar mass	$29.85 \cdot 10^{-3}$	kg/mol	[68]
a_S	Absorptivity (solid)	0.11	–	[46, 47]
a_L	Absorptivity (liquid)	0.16	–	[46, 47]

Table 6 Microscopes used in this work

Type	Manufacturer	Model
Stereo Microscope (SM)	Nikon, Japan	SMZ1500
Incident Light Microscope (ILM)	Nikon, Japan	MM40
Scanning Electron Microscope (SEM)	JEOL, Japan	JSM-IT200 InTouchScope
Scanning Transmission Electron Microscope (STEM)	Thermo Fisher Scientific, USA	Helios Nanolab 600

Table 7 Material properties for Argon at a temperature of 300 K and an ambient pressure of 100 kPa [69]

Property	Value	Unit	Reference
Density	1.603	kg/m^3	[69]
Viscosity	$2.28 \cdot 10^{-5}$	N·s/m^2	[69]
Thermal conductivity	0.01785	W/(m·K)	[69]
Specific heat capacity	520	J/(kg·K)	[69]

Table 8 Material properties of Si

Symbol	Property	Value	Unit	References
ρ_S	Density (solid)	2328	kg/m^3	[70]
ρ_L	Density (liquid)	2524	kg/m^3	[47]
T_S	Solidus temperature	1200	K	[47]
T_L	Liquidus temperature	1685	K	[47]
T_B	Boiling temperature	3250	K	[67]
k_S	Thermal conductivity (solid)	25	W/(m·K)	[47]
k_L	Thermal conductivity (liquid)	56	W/(m·K)	[47]
H_L	Enthalpy of fusion	$1877 \cdot 10^3$	J/kg	[47]
H_B	Boiling enthalpy	$14.1 \cdot 10^6$	J/kg	[67]
$c_{p,S}$	Specific heat capacity (solid)	230	J/(kg·K)	[47]
$c_{p,L}$	Specific heat capacity (liquid)	968	J/(kg·K)	[47]
η	Dynamic viscosity	$0.94 \cdot 10^{-3}$	Pa·s	[47]
α	Surface tension coefficient	0.865	N/m	[47]
H_{spec}	Specific heat of evaporation	$14.1 \cdot 10^6$	J/kg	[67]
H_{molar}	Molar heat of evaporation	$395 \cdot 10^3$	J/mol	[67]
M	Molar mass	$27.98 \cdot 10^{-3}$	kg/mol	[71]
a_S	Absorptivity (solid)	0.030	–	[46]
a_L	Absorptivity (liquid)	0.2630	–	[46, 47]

Data availability The raw data required to reproduce these findings can be requested from the corresponding author.

Declarations

Conflict of interest On behalf of all authors, the corresponding author states that there is no conflict of interest.

References

1. Attaran M (2017) The rise of 3-d printing: The advantages of additive manufacturing over traditional manufacturing. Bus Horiz 60(5):677–688

2. Aboulkhair NT, Everitt NM, Maskery I, Ashcroft I, Tuck C (2017) Selective laser melting of aluminum alloys. MRS Bull 42(4):311–319

3. DebRoy T, Wei H, Zuback J, Mukherjee T, Elmer J, Milewski J, Beese AM, Wilson-Heid A, De A, Zhang W (2018) Additive manufacturing of metallic components-process, structure and properties. Prog Mater Sci 92:112–224

4. Olakanmi EO, Cochrane R, Dalgarno K (2015) A review on selective laser sintering/melting (sls/slm) of aluminium alloy powders: Processing, microstructure, and properties. Progress Materials Sci 74:401–477

5. Martin JH, Yahata BD, Hundley JM, Mayer JA, Schaedler TA, Pollock TM (2017) 3d printing of high-strength aluminium alloys. Nature 549(7672):365–369

6. Rometsch PA, Zhu Y, Wu X, Huang A (2022) Review of high-strength aluminium alloys for additive manufacturing by laser powder bed fusion. Mater Des 219:110779

7. Montero-Sistiaga ML, Mertens R, Vrancken B, Wang X, Van Hooreweder B, Kruth J-P, Van Humbeeck J (2016) Changing the alloy composition of Al7075 for better processability by selective laser melting. J Mater Process Technol 238:437–445

8. Aversa A, Lorusso M, Cattano G, Manfredi D, Calignano F, Ambrosio EP, Biamino S, Fino P, Lombardi M, Pavese M (2017) A study of the microstructure and the mechanical properties of an alsini alloy produced via selective laser melting. J Alloy Compd 695:1470–1478

9. Zhang H, Zhu H, Nie X, Yin J, Hu Z, Zeng X (2017) Effect of zirconium addition on crack, microstructure and mechanical behavior of selective laser melted al-cu-mg alloy. Scripta Mater 134:6–10

10. Wimmer A, Kolb CG, Assi M, Favre J, Bachmann A, Fraczk-iewicz A, Zaeh MF (2020) Investigations on the influence of adapted metal-based alloys on the process of laser beam melting. J Laser Appl 32(2):022029

11. Lippold JC (2015) Welding Metallurgy and Weldability. Wiley Online Library, USA

12. Sun Z, Tan XP, Descoins M, Mangelinck D, Tor SB, Lim CS (2019) Revealing hot tearing mechanism for an additively manufactured high-entropy alloy via selective laser melting. Scripta Mater 168:129–133

13. Chauvet E, Kontis P, Jägle EA, Gault B, Raabe D, Tassin C, Blandin J-J, Dendievel R, Vayre B, Abed S et al (2018) Hot cracking mechanism affecting a non-weldable ni-based superalloy produced by selective electron beam melting. Acta Mater 142:82–94

14. Dreano A, Favre J, Desrayaud C, Chanin-Lambert P, Wimmer A, Zaeh MF (2022) Computational design of a crack-free aluminum alloy for additive manufacturing. Addit Manuf 55:102876

15. Sonawane A, Guilhem R, Blandin J-J, Despres A, Martin G (2021) Cracking mechanism and its sensitivity to processing conditions during laser powder bed fusion of a structural aluminum alloy. Materialia 100976

16. Sonawane A, Roux G, Blandin J-J, Despres A, Martin G (2021) Insights into the cracking mechanism affecting a structural aluminum alloy processed by laser powder bed fusion. AMI: Materialia

17. Stopyra W, Gruber K, Smolina I, Kurzynowski T, Kuźnicka B (2020) Laser powder bed fusion of AA7075 alloy: Influence of process parameters on porosity and hot cracking. Additive Manufacturing 101270

18. Sun Z, Chueh Y-H, Li L (2020) Multiphase mesoscopic simulation of multiple and functionally gradient materials laser powder bed fusion additive manufacturing processes. Addit Manuf 35:101448

19. Koch H, Leitz K-H, Otto A, Schmidt M (2010) Laser deep penetration welding simulation based on a wavelength dependent absorption model. Phys Procedia 5:309–315

20. Russell MA, Souto-Iglesias A, Zohdi TI (2018) Numerical simulation of laser fusion additive manufacturing processes using the sph method. Comput Methods Appl Mech Eng 341:163–187

21. Weirather J, Rozov V, Wille M, Schuler P, Seidel C, Adams NA, Zaeh MF (2019) A smoothed particle hydrodynamics model for laser beam melting of Ni-based alloy 718. Comput Math Appl 78(7):2377–2394

22. Afrasiabi M, Lüthi C, Bambach M, Wegener K (2021) Multi-resolution sph simulation of a laser powder bed fusion additive manufacturing process. Applied Sciences 11(7)

23. Fürstenau J-P, Wessels H, Weißenfels C, Wriggers P (2019) Generating virtual process maps of slm using powder-scale sph simulations. Computational Particle Mechanics

24. Lüthi C, Afrasiabi M, Bambach M (2023) An adaptive smoothed particle hydrodynamics (sph) scheme for efficient melt pool simulations in additive manufacturing. Comput Math Appl 139:7–27

25. Wimmer A, Yalvac B, Zoeller C, Hofstaetter F, Adami S, Adams NA, Zaeh MF (2021) Experimental and numerical investigations of in situ alloying during powder bed fusion of metals using a laser beam. Metals 11(11)

26. Wimmer A, Hofstaetter F, Jugert C, Wudy K, Zaeh MF (2021) In situ alloying: investigation of the melt pool stability during powder bed fusion of metals using a laser beam in a novel experimental set-up. Progress in Additive Manufacturing

27. Goetz D, Bachmann A, Wimmer A, Zaeh MF (2021) Topologieoptimierung beim Laser-Strahlschmelzen: Konzept zur Beruecksichtigung des Fertigungsprozesses. Zeitschrift fuer wirtschaftlichen Fabrikbetrieb 116(1–2):70–74

28. Rappaz M, Drezet J-M, Gremaud M (1999) A new hot-tearing criterion. Metall and Mater Trans A 30(2):449–455

29. Boettger B, Apel M, Santillana B, Eskin D (2013) Relationship between solidification microstructure and hot cracking susceptibility for continuous casting of low-carbon and high-strength low-alloyed steels: a phase-field study. Metall Mater Trans A 44(8):3765–3777

30. Bellet M, Qiu G, Carpreau J-M (2016) Comparison of two hot tearing criteria in numerical modelling of arc welding of stainless steel aisi 321. J Mater Process Technol 230:143–152

31. Song J, Pan F, Jiang B, Atrens A, Zhang M-X, Lu Y (2016) A review on hot tearing of magnesium alloys. J Magnesium Alloys 4(3):151–172

32. Kou S (2015) A criterion for cracking during solidification. Acta Mater 88:366–374

33. Kou S (2015) A simple index for predicting the susceptibility to solidification cracking. Weld J 94:374–388

34. Hu XY, Adams NA (2006) A multi-phase SPH method for macroscopic and mesoscopic flows. J Comput Phys 213(2):844–861

35. Adami S, Hu XY, Adams NA (2013) A transport-velocity formulation for smoothed particle hydrodynamics. J Comput Phys 241:292–307

36. Cleary PW, Prakash M, Ha J (2006) Novel applications of smoothed particle hydrodynamics (SPH) in metal forming. J Mater Process Technol 177(1–3):41–48

37. Cleary PW (2010) Extension of SPH to predict feeding, freezing and defect creation in low pressure die casting. Appl Math Model 34(11):3189–3201

38. Adami S, Hu XY, Adams NA (2012) A generalized wall boundary condition for smoothed particle hydrodynamics. J Comput Phys 231(21):7057–7075

39. Zhou J, Zhang Y, Chen J (2009) Numerical simulation of random packing of spherical particles for powder-based additive manufacturing. Journal of manufacturing science and engineering 131(3)

40. Incardona P, Leo A, Zaluzhnyi Y, Ramaswamy R, Sbalzarini IF (2019) Openfpm: A scalable open framework for particle and particle-mesh codes on parallel computers. Comput Phys Commun 241:155–177

41. Swope WC, Andersen HC, Berens PH, Wilson KR (1982) A computer simulation method for the calculation of equilibrium constants for the formation of physical clusters of molecules: Application to small water clusters. J Chem Phys 76(1):637–649

42. Monaghan JJ (1992) Smoothed particle hydrodynamics. Ann Rev Astron Astrophys 30(1):543–574

43. Cleary PW, Monaghan JJ (1999) Conduction modelling using smoothed particle hydrodynamics. J Comput Phys 148(1):227–264

44. Morris JP (1996) A study of the stability properties of smooth particle hydrodynamics. Publ Astron Soc Austral 13:97–102

45. Zöller C, Adams N, Adami S (2023) A partitioned continuous surface stress model for multiphase smoothed particle hydrodynamics. J Comput Phys 472:111716

46. Bramson MA (1968) Infrared radiation: a handbook for applications, with a collection of reference tables

47. Valencia JJ, Quested PN (2008) Thermophysical properties. ASM Handbook 15:468–481

48. Mills KC (2002) Recommended Values of Thermophysical Properties for Selected Commercial Alloys. Woodhead Publishing, UK

49. Saunders N, Miodownik AP (1998) Calphad (calculation of phase diagrams): a comprehensive guide. Elsevier, Netherlands

50. Scheil E (1942) Bemerkungen zur schichtkristallbildung. Z Met 34(3):70–72

51. Gulliver G (1913) The quantitative effect of rapid cooling upon the constitution of binary alloys. J Inst Met 9(1):120–157

52. Eskin D, Katgerman L (2007) A quest for a new hot tearing criterion. Metall and Mater Trans A 38:1511–1519

53. Sheng Y, Zhi W, Feng W, Zheng L, Pingli M, Xiaoping J (2018) An investigation on hot tearing of az91 alloys with yttrium additions. Materials Research Express 6(1):016554

54. Jia D, Liu Z, Mao P, Wang F, Wang Z (2017) Hot tearing behavior of mg–5 (zn+ y)–0.5 zr alloys. Materials Research Express 4(10):106511

55. Hai-kuo D, Feng W, Zhi W, Jin-kun L, Zheng L, Ping-li M (2018) Effect of sn addition on hot tearing susceptibility of axj530 alloy. Materials Research Express 5(3):036513

56. Bakir N, Gumenyuk A, Rethmeier M (2018) Investigation of solidification cracking susceptibility during laser beam welding using an in-situ observation technique. Sci Technol Weld Joining 23(3):234–240

57. Niel A, Bordreuil C, Deschaux-Beaume F, Fras G (2013) Modelling hot cracking in 6061 aluminium alloy weld metal with microstructure based criterion. Sci Technol Weld Joining 18(2):154–160

58. Bodaghi F, Movahedi M, Kokabi A, Tavakoli R (2019) Effect of solid fraction, grain misorientation and grain boundary energy on solidification cracking in weld of Al-Cu aluminum alloys. Materials Research Express 6(8):086598

59. Dahle A, StJohn D (1998) Rheological behaviour of the mushy zone and its effect on the formation of casting defects during solidification. Acta Mater 47(1):31–41

60. Shrestha S, Chou K (2018) Single track scanning experiment in laser powder bed fusion process. Procedia Manufacturing 26:857–864 (46th SME North American Manufacturing Research Conference, NAMRC 46. Texas, USA)

61. Nayak SK, Mishra SK, Paul CP, Jinoop AN, Bindra KS (2020) Effect of energy density on laser powder bed fusion built single tracks and thin wall structures with 100 preplaced powder layer thickness. Optics Laser Techn 125:106016

62. Otani Y, Sasaki S (2020) Effects of the addition of silicon to 7075 aluminum alloy on microstructure, mechanical properties, and selective laser melting processability. Mater Sci Eng, A 777:139079

63. Smith WF, Hashemi J, Presuel-Moreno F (2006) Foundations of Materials Science and Engineering vol. 509. McGraw-hill New York, ???

64. Massalski TB, Okamoto H (1990) Binary Alloy Phase Diagrams vol. 1. ASM International, Materials Park, ???

65. Technical data sheet en aw 7075. Technical report, Aluminium Giesserei Hannover GmbH (2020). Aluminium Giesserei Hannover GmbH

66. Technical data sheet en aw 7075. Technical report, Gleich GmbH (2020). Gleich GmbH

67. Zhang Y, Evans JR, Yang S (2011) Corrected values for boiling points and enthalpies of vaporization of elements in handbooks. J Chem Eng Data 56(2):328–337

68. Meija J, Coplen TB, Berglund M, Brand WA, De Bièvre P, Gröning M, Holden NE, Irrgeher J, Loss RD, Walczyk T et al (2016) Atomic weights of the elements 2013 (iupac technical report). Pure Appl Chem 88(3):265–291

69. Ahlberg K (1985) Aga gas handbook. AGA AB

70. Conwell EM (1952) Properties of silicon and germanium. Proc IRE 40(11):1327–1337

71. Audi G, Wapstra AH, Thibault C (2003) The AME2003 atomic mass evaluation: (II). tables, graphs and references. Nucl Phys A 729(1):337–676